Combined three-point bending and axial tension of pressurised and unpressurised X65 offshore steel pipes – experiments and simulations

Martin Kristoffersen[a,*], Magnus Langseth[a], Tore Børvik[a]

[a]*Structural Impact Laboratory (SIMLab), Department of Structural Engineering, Centre for Advanced Structural Analysis (CASA), Norwegian University of Science and Technology NTNU, Rich. Birkelands vei 1A, NO-7491 Trondheim, Norway*

Abstract

Subsea pipelines are occasionally struck and hooked by objects such as anchors or trawl gear. The initial denting, followed by potential hooking and displacement of the pipeline, give rise to a complex load and deformation history. Transverse displacements cause a simultaneous increase in tensile axial forces, further complicating the load sequence. This study examines the effect of applying one of three different axial loads (zero, constant, and linearly increasing) to a pipe while simultaneously deforming it transversely. The three tests were repeated with an internal pressure of 10 MPa (100 bar), and all tests were recreated numerically in finite element simulations using both iterative (implicit) and non-iterative (explicit) approaches. As expected, adding an axial load increased the pipe's resistance to bending in terms of force-displacement, and the same can be said of including internal pressure. However, a more localised dent was observed in the pressurised pipes, which in turn could affect the onset of failure. The experimental results were well captured by the finite element simulations.

Keywords: pipe impact, material tests, combined loading, stretch-bending tests, finite element simulations

1. Introduction

Pipelines are a crucial part of the offshore industry, and will remain so for the foreseeable future. Along the seabed, pipelines may be exposed to various hazards [1], among them being impact, hooking and release of the pipeline by e.g. anchors or trawl gear [2, 3], which is treated in the DNV GL guidelines [4]. This load cycle causes a complex stress and strain history which in turn may lead to fracture [5]. The load sequence of denting followed by stretching was applied quasi-statically to strips of an X65 pipeline material by Manes et al. [6], without producing any significant cracks. Further, Kristoffersen et al. [7] carried out dynamic impact tests on simply supported pipes followed by quasi-static stretching of the dented pipes to emulate the rebound of a pipeline after release from a hooking event. The subsequent stretching always resulted

*Corresponding author, tel.: +47-73-59-46-66; fax: +47-73-59-47-01
Email address: martin.kristoffersen@ntnu.no (Martin Kristoffersen)

in fracture in the material, ranging from surface cracks to through-thickness cracks. When a pipeline is displaced transversely, an axial force builds up simultaneously [8], and this was not accounted for in the experimental procedure by Kristoffersen et al. [7]. The current study includes experiments that encompass the tensile force caused by the transverse displacement.

The open literature provides many studies on transverse loading of tubular structures of various character, ranging from rectangular cross-sections [9] to more complicated T-joints [10]. Circular cross-sections are the most common, and have been studied experimentally [11, 12], theoretically [13] and numerically [14]. Pipe impact problems have been studied with various boundary conditions, from simply supported pipes [15] to fully clamped pipes [16–18] and pipes resting on a foundation [19]. Pipeline coating intended for ballast or thermal insulation, usually made from concrete [20] or polymers [21], also offer some protection from impact loads. Combinations of axial loading and bending moment have been examined in several studies [22–25], where load history, anisotropy, diameter to thickness ratio, and other parameters are discussed. While some works consider the effect of external pressure on tubular structures [26–29], this work will consider internal pressure caused by e.g. an internal fluid or gas. Internal pressure can reduce the ovalisation of the cross-section [30], and simultaneously increase the resistance load during denting and transverse deformation [31, 32]. Large transverse displacements combined with a tensile axial load and internal pressure have not, to the best knowledge of the authors, been studied in detail previously. In addition to providing experimental data on this problem, an elaborate numerical study is also carried out herein.

This work investigates the local indentation and subsequent bending of an uncoated X65 steel pipe due to a transverse load [33], while simultaneously applying one of three axial tensile loads: 1) no axial load, 2) a constant axial load, or 3) a linearly increasing axial load. These three cases are then repeated with an internal pressure of about 10 MPa, amounting to six different stretch-bending tests in total. The order in which the loads are applied can affect the results [23, 34, 35], but in this case the pipe is assumed to be in operation when being deformed, meaning that the pressure is applied before the transverse and axial loading. These experiments were recreated numerically using the finite element sofware ABAQUS [36] with a calibrated and tested material model [37]. A comprehensive numerical study is conducted using different numerical approaches (iterative versus non-iterative), and some suggestions for modelling this type of problem are made. In general, the experimental results were well captured by the numerical simulations.

2. Material characterisation

2.1. Description

The pipeline material used in this study is an X65 grade offshore steel, a material widely used in pipelines conveying oil and/or gas [38]. According to the material inspection certificate, the nominal yield strength is $\sigma_0 = 450$ MPa and the ultimate tensile strength is $\sigma_{\mathrm{UTS}} = 535$ MPa. Young's modulus is $E_s = 208\,000$ MPa.

The pipes used herein are made seamless by utilising the Mannesmann effect [39], and are supplied by Tenaris, Argentina.

2.2. Material tests

Quasi-static material tests investigating the cross-sectional homogeneity and possible anisotropy of this material have been carried out [7], and are succinctly summarised here. Specimens of geometry as shown in Fig. 1(a) were loaded to failure in tension at quasi-static strain rate (approximately 10^{-3} s^{-1}). By using a laser-based measuring device [40], the minimum diameters in perpendicular directions were recorded continuously during testing. This provides the true stress-true plastic strain curve beyond necking, and data from a typical test is shown in Fig. 1(b). A detailed characterisation of the material is important in order to obtain accurate analyses [41].

For engineering and design purposes, the material is found to be both homogeneous and isotropic. Based on values from 12 tests, the material yields at 478 ± 15 MPa and has an engineering peak stress of 572 ± 14 MPa. The material strain hardens to a true peak stress of $1\,314 \pm 12$ MPa and fails at a true strain of 1.61 ± 0.03 in a ductile cup-and-cone fracture mode. This study does not include investigation of fracture, which has been studied elsewhere [7, 42]. All tests (both material and component) are carried out at room temperature, so no investigation into temperature effects is made although such effects may be present in both arctic environments and dynamic events [43].

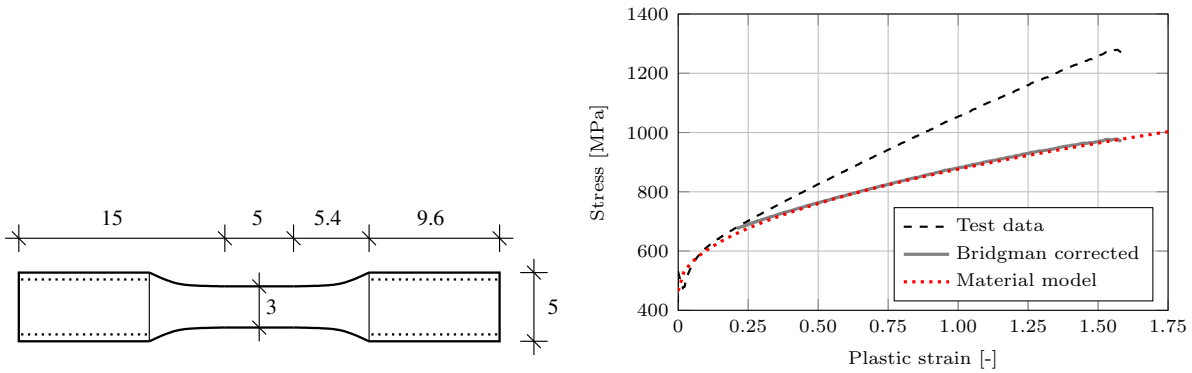

(a) Specimen geometry in mm

(b) Stress-plastic strain curves

Fig. 1: Tensile test data, where (a) shows the specimen geometry while (b) shows a representative stress-plastic strain curve from the tests along with Bridgman corrected data and a power law fit.

2.3. Constitutive relation

J2 flow theory is used to model the X65 material. This means that the von Mises yield criterion is employed with the associated flow rule. Only isotropic hardening R_H is considered, here represented by a

power-law. The von Mises equivalent stress σ_{eq} is given as a function of the deviatoric part $\boldsymbol{\sigma}^{\text{dev}}$ of the Cauchy stress tensor $\boldsymbol{\sigma}$,

$$\sigma_{\text{eq}}\left(\boldsymbol{\sigma}\right) = \sqrt{\frac{3}{2}\,\boldsymbol{\sigma}^{\text{dev}} : \boldsymbol{\sigma}^{\text{dev}}} \tag{1}$$

The strain hardening R_H is expressed as

$$R_H\left(\varepsilon_{\text{eq}}\right) = R_0 \varepsilon_{\text{eq}}^{n} \tag{2}$$

where ε_{eq} is the equivalent plastic strain, and R_0 and n are the strain hardening constants. The initial size of the yield surface, i.e., when the equivalent plastic strain is zero, is given by the constant σ_y. As the tests conducted herein are carried out at quasi-static strain rates, no strain rate effects are accounted for in the constitutive relation. Also, isothermal conditions are assumed. Then, from Eq. (1) and Eq. (2), the yield function f becomes

$$f\left(\boldsymbol{\sigma}, \varepsilon_{\text{eq}}\right) = \sigma_{\text{eq}} - \left(\sigma_y + R_H\right) \leq 0 \tag{3}$$

The material constants are taken from a study using the exact same pipe material [44], and are listed in Table 1 where ν is the Poisson ratio and ρ_s is the density. Bridgman's analysis [45] and an empirical relation [46] were used to obtain the equivalent stress from the measured major principal stress, and a least squares approach was employed to fit the constants σ_y, R_0 and n to the Bridgman corrected data. Fig. 1(b) shows the Bridgman corrected data along with the least squares fit. No failure criterion has been used in this study as the pipe specimens showed no signs of fracture after the applied load sequences.

Table 1: X65 steel material constants used in numerical simulations [44].

Elasticity and density			**Yield stress, strain hardening**		
E_s [MPa]	ν [-]	ρ_s [kg/m^3]	σ_y [MPa]	R_0 [MPa]	n [-]
208 000	0.33	7800	465.5	410.8	0.479

3. Component tests

3.1. Setup of experiments

It is difficult to apply a controlled axial load while maintaining a constant internal pressure during a highly dynamic and transient pipe impact test, especially if the relative decrease of volume in the pipe is large. With these difficulties in mind and for safety reasons, the component tests herein are carried out at quasi-static deformation rates.

The pipes were initially about 10 mm thick, but were lathed down to about 4 mm in the test section to obtain a diameter to thickness ratio of approximately 30. This ratio was chosen because it is similar to a real case from the North Sea, where a pipeline was impacted and hooked by an anchor which caused at least a 53 m transverse displacement [47]. The diameter to thickness ratio affects the collapse behaviour of pipes highly [24], and a low ratio may invoke strengthening membrane forces at an earlier stage of the lateral deformation [13]. In this study, however, the ratio is locked to only one configuration to keep the number of parameters at manageable level.

An ultrasound device was used to measure the thickness of each pipe across a grid which spanned over the 1000 mm long lathed test section of the pipe. The average thickness and standard deviation from these measurements are given in Table 2 for each pipe. The inner diameter of the pipes is 123 mm, and the initial span between the rotation points (RP) on the test rig is 2146 mm, whereas the specimens themselves were only 1250 mm long initially. The additional length to the span comes from the somewhat convoluted connection required to fit the circular geometry of the pipes to the test rig and allow for application of an internal pressure.

A test rig capable of applying an axial load while at the same time bending a specimen transversely [48] has been used to test the X65 steel pipes, and the rig is shown in Fig. 2. Two horizontal hydraulic actuators apply the axial load N_a, while a third bends the pipe transversely (three-point bending) using deformation control. As a pointed impactor perforates a pipe more easily [49], the sharpest geometry (nose radius

Table 2: Test matrix of pipes subjected to combined quasi-static stretching and bending. See Fig. 3 for legend and illustration.

Pipe		**A1**	**A2**	**A3**	**P1**	**P2**	**P3**
Nose radius	[mm]	10	10	10	10	10	10
Transverse def.	[mm]	200	200	200	200	200	200
Avg. thickness	[mm]	4.19±0.19	4.19±0.26	4.06±0.23	4.08±0.24	3.95±0.21	4.13±0.18
Nom. overpressure	[MPa]	0	0	0	10.0	10.0	10.0
Nom. axial load	[kN]	0	53	0-53	0	53	0-53
				Test results			
Transverse def.	[mm]	197	201	202	200	200	200
w_i	[mm]	120	120	122	117	159*	113
ΔL	[mm]	31	24	25	32	27	26
$L_{\text{N-N}}$	[mm]	1200	1197	1198	1200	1168*	1200
Force at "peak"	[kN]	40.7	45.9	40.6	47.5	-	-
Force at end of test	[kN]	40.7	47.0	45.7	45.0	61.1	65.4
α	[deg]	8.7	8.5	8.7	9.6	11.6*	9.2
Avg. axial force	[kN]	0.5†	53.0	-	0.5†	53.2	-
Avg. overpressure	[MPa]	0	0	0	10.3	10.3	10.1
$d_{\text{N-S}}$	[mm]	84	89	87	98	90*	97
$d_{\text{E-W}}$	[mm]	164	165	164	152	164*	152

*Post-test geometric measurements are inaccurate due to an erroneously applied compressive force after the test.

†Force required to pull the horizontal pistons out.

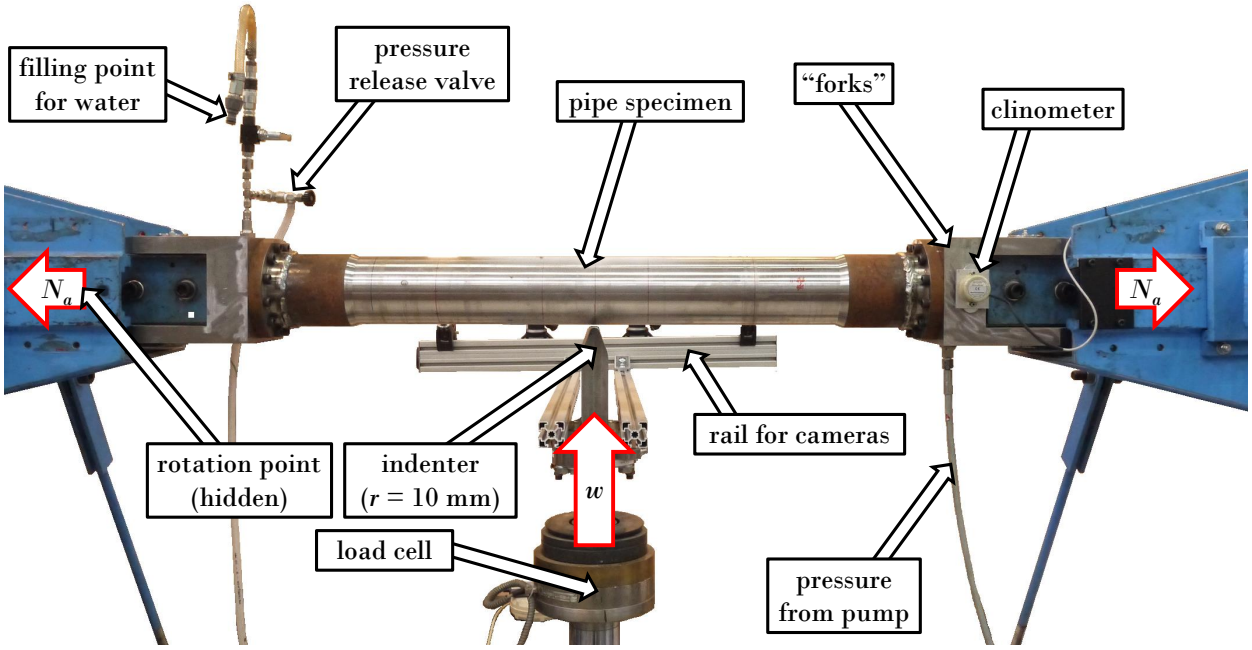

Fig. 2: Pipe specimen mounted in stretch-bending rig, where the indenter deforms the pipe transversely. The axial load N_a is applied at the rotation points, which are hidden behind structural parts of the rig. The transverse deformation w is vertical as indicated by the arrow, and load cells register both the transverse and axial forces.

r = 10 mm) from the guidelines [4] is chosen for the indenter. Although the size and orientation of the indenter can be influential [50], this study is restricted to only one indenter configuration. The applied transverse displacement is 200 mm at a rate of 25 mm/min in all cases, while the axial load varies between three cases: 1) no axial load, 2) a constant axial load of about 53 kN, and 3) an axial load increasing linearly from zero to 53 kN simultaneously as the transverse displacement increases from zero to 200 mm. The value of the applied axial load was based on simplified beam calculations, and is well below the elastic limit $N_{\text{el}} \approx 718$ kN estimated by

$$N_{\text{el}} = \sigma_0 \, A_t \tag{4}$$

in which A_t is the cross-sectional area of the test section of the pipe.

The first three cases will be tested without pressure (pipes A1-A3), before the same three cases are repeated with an internal pressure p of about 10 MPa (pipes P1-P3). The component test matrix is shown in Table 2, along with some experimental results. The results will be explained in detail in Section 3.2. A sketch of a deformed pipe is shown in Fig. 3. The following test procedure is used for each pipe:

1. Application of internal pressure (if relevant).
2. Application of constant horizontal load (if relevant).

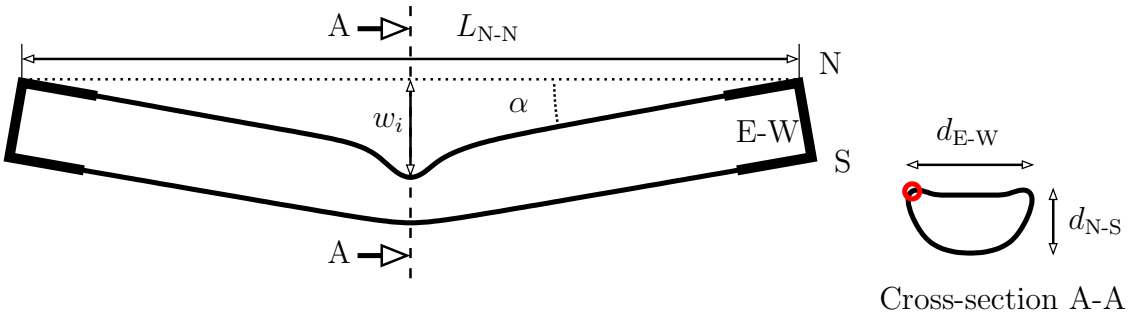

Fig. 3: Typical outline of deformation shape (not to scale) of pipes after testing, along with explanation of measurements given in Table 2.

3. (a) Application of transverse displacement of 200 mm.
   (b) Application of linearly increasing horizontal load (if relevant).
4. Locking of horizontal actuators.
5. Removal of vertical indenter.
6. Release of horizontal actuators.

If a constant axial force is used, it is applied before the transverse deformation. If a linearly increasing axial load is used, then it is increased along with the transverse deformation, i.e., both the axial force and the deformation increase simultaneously from zero to the maximum prescribed value (53 kN and 200 mm, respectively) during the same time interval (approximately 480 s). Water was used to pressurise the pipes by utilising a pump continuously working throughout the test procedure. A pressure release valve opening automatically at approximately 10.2 MPa kept the pressure in the system constant – this was necessary as the volume of the pipes decreases markedly during deformation. The water was filled from the top (the filling point is shown in Fig. 2) to minimise the amount of trapped air inside the pipe. During testing, the horizontal and vertical forces and displacements were logged. As were the angle α at the pipe ends, and the final measurements of the angles after the test procedure are presented in Table 2. The force at the first "peak", occuring just before 50 mm displacement in Fig. 4, is also listed in the table for each pipe. Pressure sensors logged the pressure inside the pipe. After the pipe has been deformed transversely, the distance between the rotation points at each end contracts somewhat and this contraction is called ΔL in Table 2.

3.2. Experimental results

Fig. 3 shows a typical outline of a deformed pipe, and serves as a legend for several measurements in Table 2. As the indenter makes contact with the pipe, a plastic hinge is formed which starts at the contact point and moves to each side down the pipe's cross-section. The final position of the plastic hinge is shown in

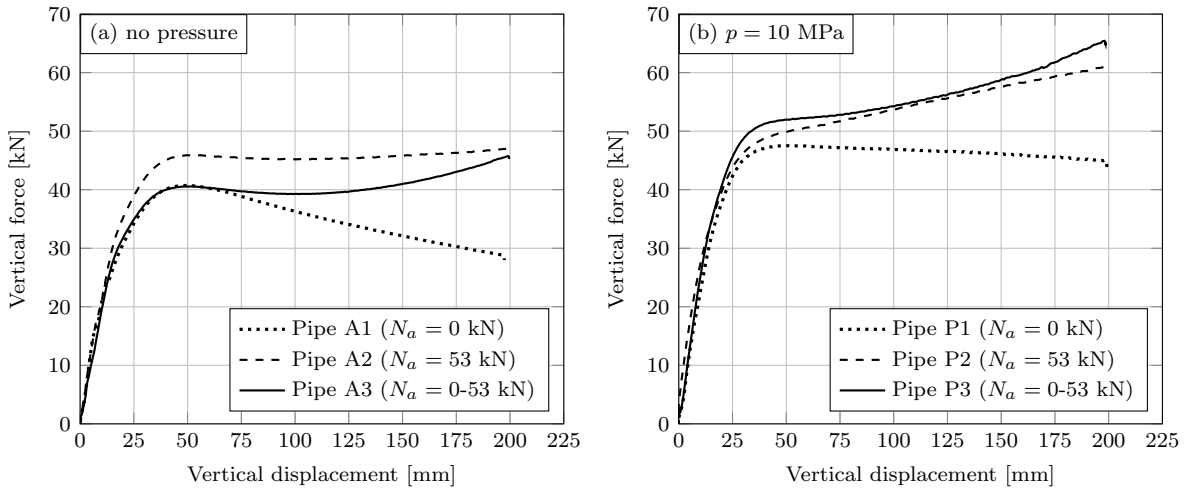

Fig. 4: Transverse force-displacement curves from (a) the unpressurised pipes A1-A3, and (b) the pressurised pipes P1-P3.

a red circle in Fig. 3. Transverse force-displacement curves are shown in Fig. 4 [1], with part (a) containing the data from the experiments without internal pressure, and part (b) showing the resulting force-displacement curves when an additional internal pressure of about 10 MPa is applied to the pipe. As expected, the stiffness – i.e., the initial slope of the force-displacement curves – is higher when internal pressure is included. After 25 mm deformation, the force is above 40 kN for all pressurised pipes while for the unpressurised pipes it is about 35 kN. The general force level is increased by including internal pressure, providing an additional resistance to bending. The pressure p acting on the end caps gives rise to an internal stress σ_p in the axial direction of the pipe. Assuming a thin-walled pipe, σ_p can be estimated by [51]

$$\sigma_p = p \, \frac{A_{\text{end}}}{A_t} \tag{5}$$

where A_{end} is the area of the end cap, which the pressure p acts upon. With an internal diameter of $D_i = 123$ mm σ_p becomes about 76 MPa which is well below the yield stress, and the hoop stress is twice of σ_p. Thus, the axial stress causes a small elongation of the pipe, but no constraint forces arise as the horizontal pistons are free to move during the build up of the internal pressure. When an external axial force N_a is applied by the pistons, this adds further stresses to the pipe in the axial direction. The maximum value of N_a is 53.5 kN, which adds a stress $\sigma_a = N_a/A_t = 34$ MPa. The axial stress is then about 110 MPa, roughly a quarter of the nominal yield stress.

From Fig. 4 it is judged that a constant axial load increases the pipe's resistance to bending, i.e., the force required to produce an equivalent deformation without the axial load is lower. The linearly increasing

[1] The data for pipe P3 was subject to an offset error when presented at the OMAE 2017 conference [33], and this has been corrected for this publication.

axial load has the same effect, and the effect is greater for larger values of the applied axial load as one would expect. In terms of final dent deformation, it was hard to distinguish between the three different tensile axial loads. The local cross-sectional deformation thereby appears much less affected by the axial load than by the internal pressure. Still, the difference in distance between the rotation points before and after testing ΔL decreased somewhat with increasing axial force (see Table 2). On the other hand, a compressive axial load (not investigated herein) can reduce the lateral collapse load significantly [52]. The reason for pipe P3 having a higher force level than P2 is mainly attributed to differences in pipe wall thickness.

A pronounced difference in cross-sectional deformation is noted when internal pressure is applied, resulting in smaller values of $d_{\text{E-W}}$ and larger values of $d_{\text{N-S}}$ (legend shown in Fig. 3). The dent becomes more localised as depicted in Fig. 5, where the top row shows the dent in the pipe after being deformed without internal pressure, and the bottom row with internal pressure. This may of course alter not only the magnitude of strains but also the strain path, which can be quite important when discussing potential fracture [42]. A much rounder final cross-sectional deformation is noted for the pressurised pipes, as also noted by others [53, 54]. The dent depth becomes smaller and the curvature around the dent is higher, thus conforming with results from previous studies [30, 31, 55]. Smaller cross-sectional deformation is beneficial, because when a dent exceeds 5% of the outer diameter the load bearing capacity reduces quickly [56]. The dent profile is, however, constrained to a smaller area as observed in Fig. 5. This could change the level

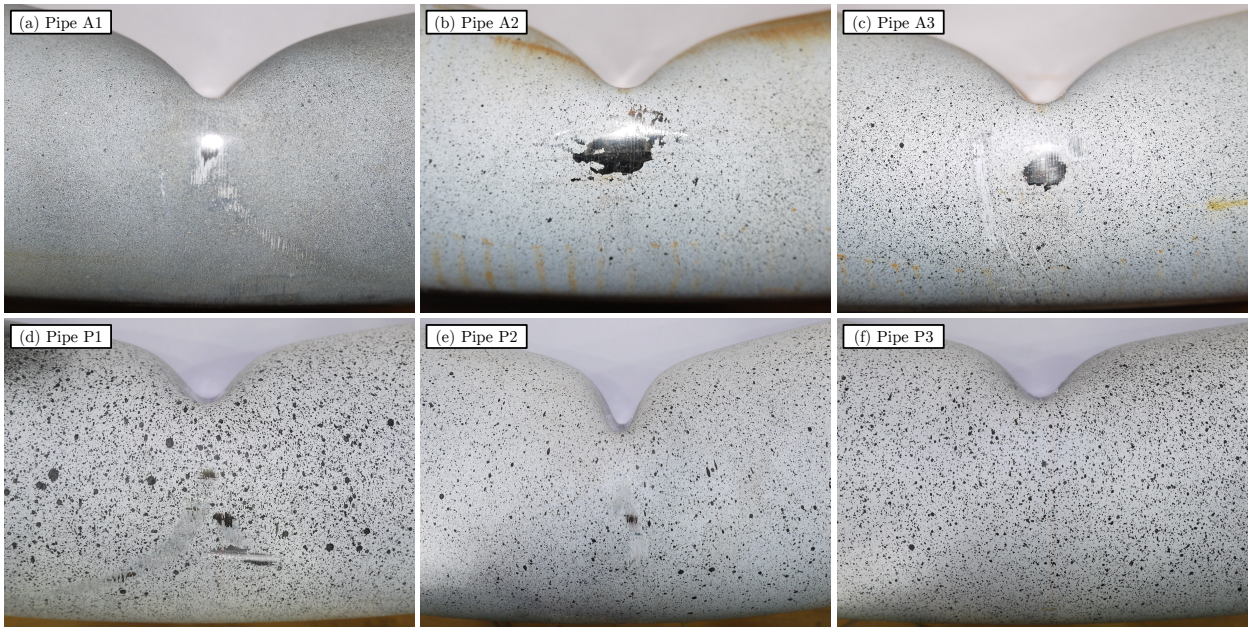

Fig. 5: Local deformation in dent without pressure (top row) and with 10 MPa internal pressure (bottom row). The left column has no axial load, the middle column has a constant axial load, while the right column has a linearly increasing axial load. The paint dots seen were applied as contrast for a digital image correlation technique.

of compression and the state of stress in the dent, which in turn may affect the probability of failure at a later stage [42]. Industry practice rarely allows deformation beyond 5% of the diameter before assuming rupture. Pipe A1 herein sufferend a dent depth of approximately 40 mm, which is approximately 30% of the diameter. While collapse may be imminent if a compressive load is added, the pipes showed no signs of fracture through the hull (discussed in more detail below). A dynamically applied load would, however, most likely alter this. Key figures from the tests are summarised in Table 2.

After the test sequence was carried out, a compressive axial force was erroneously applied to pipe P2 due to a bug in the rig's software. This caused the dent to become somewhat more compressed, as can be seen in Fig. 5(e). For this reason, a direct comparison of the measured cross-sectional deformation measured from pipe P2 with values from the other pipes is not applicable.

A digital image correlation (DIC) technique was tested on the pipes. As seen in Fig. 5, a speckled paint pattern was applied to the pipe to provide contrast for the images. Cameras were attached to the indenter so the deformation could be followed more closely. The DIC procedure has been applied with success previously, for both large [57] and small deformations [58]. In short, the procedure works by finding a correlation between a reference image and the current image by optimising a set of degrees of freedom for a pixel subset (details available in Ref. [59]). Based on the correlation it is possible to calculate the strains on the surface of the pipe.

Fig. 6(a) shows the estimated surface strains from pipe A2 at the end of the test. The maximum measured strain value in the tests was approximately 0.225. It was difficult to distinguish the six different tests based on the strain measurements alone because all the DIC analyses gave similar results. This result is most likely due to the fact that the most interesting and most strained area of the pipe – the area underneath

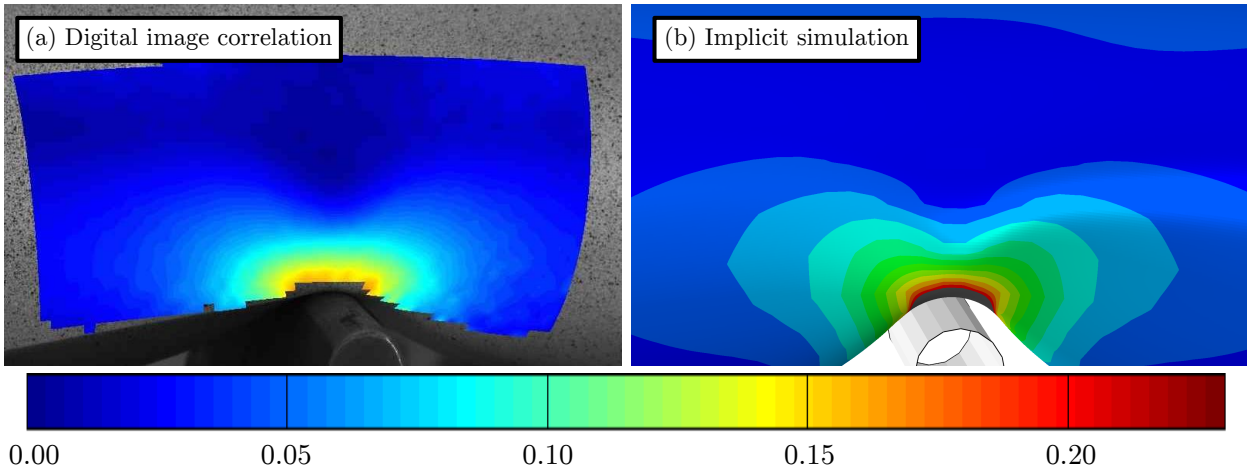

Fig. 6: Equivalent plastic strain on the surface of pipe A2 as estimated by (a) DIC, and by (b) the outermost integration points in an implicit finite element analysis using 8-noded shell elements. The strains are shown for maximum transverse deformation (200 mm).

the indenter – is not visible during the test. In addition, the bulge just above the indenter has a notable out-of-plane deformation. This causes the area to come out of focus, rendering proper correlation difficult. The curved surface of pipes were also problematic due to reflections at different angles caused different light intensity across the circumference. As can be seen in Fig. 5, the paint cracked and flaked off during some of the tests. To limit this problem, the paint should be freshly applied and not allowed to dry before testing. Finally, shadows from particularly the indenter obfuscated central areas of the pipe further.

Despite these difficulties, the DIC analyses gave decent results. They were consistent among the pipes, and the numerical simulations (discussed in detail later) gave matching results, as shown in Fig. 6(b). Both the shape and magnitude of the strain distribution are similar for the experimentally and numerically obtained values. In the numerical fringe plot, all strain values above 0.225 are hatched in dark gray to obtain the same color legend for both data sets.

The deformed pipe profiles are shown in Fig. 5, where it is evident that the material is heavily compressed at the bottom of the dents. As signs of fracture have been observed inside the pipe wall for a similar dynamic load case [5], specimens were cut from the pipes for investigation in an optical light microscope. The specimens were polished and etched in nital to reveal the microstructure.

Fig. 7(a) shows the undeformed microstructure, which is ferritic with a typical grain of approximately 10 μm or less. The grain structure is similar in the longitudinal and radial directions [7], which is reflected in the isotropic mechanical behaviour of the material. The dark areas seen are probably oblong MnS particles which retain their shape even after forming the pipes. Part (b) shows the microstructure in the compressed zone of the dent, where the grains have been elongated perpendicularly to the compressive direction, which runs left to right. The particles seen here are spherical CaAl particels which bonded poorly with the

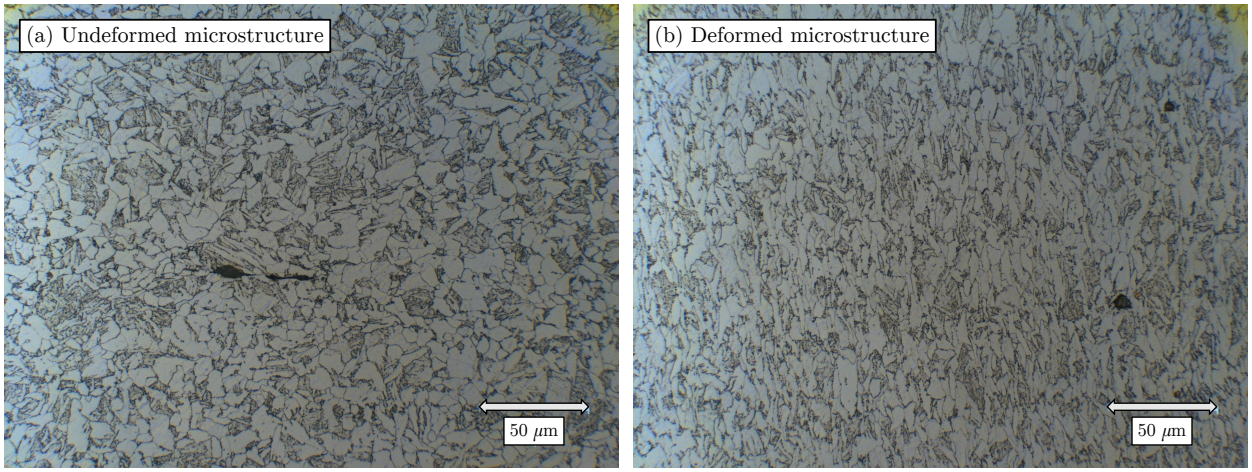

Fig. 7: Images from an optical light microscope study of the microstructure of pipe A1, where (a) shows the undeformed microstructure, and (b) the deformed microstructure in the bottom of the dent (the compressive direction is left to right).

matrix [7]. Still, no fracture was observed, even close to the particles (dark areas) where fracture is typically found in this material [42]. The absence of fracture is most likely due to the quasi-static deformation rate in both the loading and unloading phase. During an impact event against a pipe, fracture typically takes place during the rapid unloading (springback) of the pipe after attaining maximum deformation [30, 60]. In addition, the material (in its virgin state) is very ductile, with an average true failure strain of 1.61.

4. Numerical simulations

The numerical setup, seen in Fig. 8, is largely a recreation of the experimental setup, and this has been done using the commercially available finite element solver ABAQUS [36]. Even though the material exhibits strain rate sensitivity [44], this effect is omitted as the tests herein are quasi-static. With a fairly time consuming experimental procedure involving contact, the optimal numerical setup is not immediately obvious. The use of an explicit scheme offers better handling of contact at the cost of small time steps due to conditional stability. Mass or time scaling can help reduce the number or increments required to reach the termination time, but may introduce a sizable amount of kinetic energy to the system.

An implicit scheme can apply larger time steps, but they are costly due to inversion of full matrices and convergence is not necessarily guaranteed as contact can be challenging to handle. In addition, rather small time steps are required due to large plastic strain and strain gradients. Both the explicit and implicit techniques in ABAQUS will be tested while evaluating pros and cons. The explicit solution is propagated by the central difference time integration rule, whereas the implicit simulations employ a full Newton-Raphson approach for the equilibrium iterations. As no fracture was observed in the tests, no fracture criterion is included in the numerical studies herein.

Two techniques for including the pressure are also tested. The first is a direct approach where the pressure is applied as a uniformly distributed load to the internal surfaces of the pipe, while the second models the fluid and adhering pressure using an Eulerian mesh. This latter technique is only available in ABAQUS/Explicit.

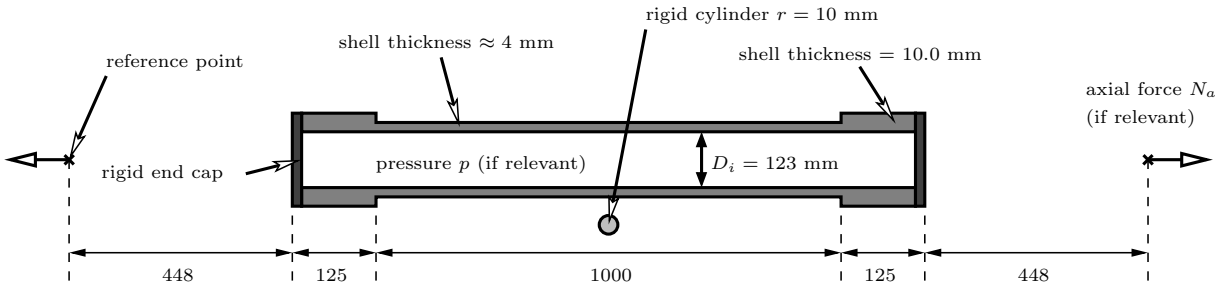

Fig. 8: Sketch of setup of finite element simulations (not to scale).

4.1. Setup of simulations

Four-node, reduced integration shell elements (called `S4R` in ABAQUS) with five integration points in the thickness direction are used to model the pipe unless otherwise stated. Shell elements are able to capture the main physics of deforming tubular structures [61], and were chosen for faster computation and for easier adjustment of the thickness of each pipe. The midsection of the pipe has a uniform shell thickness of about 4 mm (different for each pipe), while the end sections are 10 mm thick (cf. Fig. 8). At each end section a rigid end cap is attached to emulate the stiff "forks" (shown in Fig. 2) connecting the pipe to the hydraulic pistons. Reference points for these rigid caps are made to coincide spatially with the rotation points in the rig. These points are restricted to move only in the axial direction of pipe, representing the movement of the pistons. When relevant, axial loads are applied to these points. The boundary conditions are naturally quite important [62], and should not be oversimplified.

Contact is important to include, as applying nodal deformations or concentrated loads can yield non-conservative results [52]. A contact surface ranging 200 mm is created at midspan of the pipe (100 mm to each side from the center). Rigid shell elements making a cylinder with radius 10 mm were chosen to represent the indenter, a representation which has been shown to work well [33]. It is placed 1 mm above the pipe, and given a constant velocity of 0.42 mm/s throughout the analyses like in the experiments. The simulated time is 480 s, which makes the final displacement of the top of the pipe about 200 mm (200.6 mm to be exact). While traveling this distance the indenter promptly deforms the pipe through a contact pair. The force arising in this interaction is logged and compared with the experimental data. When relevant, internal pressure is applied as a uniformly distributed pressure load or by an Eulerian mesh to all internal faces of the pipe, and ramped up smoothly during 10 s before the indenter moves. During this time, the constant axial load is applied if relevant (pipes A2 and P2).

4.2. Mass scaling for explicit simulations

Quasi-static deformation rates result in time comsuming explicit simulations (see Table 3), necessitating some degree of mass scaling for these analyses. Pipe A1 is discretised by a rather coarse mesh with 16 elements around the circumference and 42 along the longitudinal axis of the 4 mm thick and 1000 mm long

Table 3: Results from mass scale study on pipe mesh with 16×42 elements using pipe A1 as a case.

Factor M	**Iterations**	F_{peak} [kN]	$\bar{F}$ [kN]	$\Delta\bar{F}$ [kN]	$\Delta\bar{F}/F_{\text{peak}}$	$E_{\text{kin}}/E_{\text{tot}}$	**Time** [hh:mm:ss]
1	134 508 429	45.8	37.7	0.0	0.0%	0.0%	36:58:03
10^2	13 450 905	45.9	37.7	0.1	0.3%	0.0%	03:55:51
10^4	1 396 965	46.8	37.8	0.3	0.8%	0.0%	00:20:05
10^6	134 206	48.6	38.0	1.0	2.6%	0.8%	00:02:17
10^8	13 378	80.6	38.6	5.8	15.0%	70.1%	00:00:12

midsection, and this case is used for the mass scaling simulations. An estimate for the critical time step Δt_{cr} is given by the length ℓ_e of the smallest element

$$\Delta t_{\text{cr}} = \frac{\ell_e}{c_s} \tag{6}$$

where c_s is the speed of sound in the material,

$$c_s = \sqrt{\frac{E_s}{\rho_s}} \tag{7}$$

in which E_s is Young's modulus and ρ_s is the mass density. With 16 elements around the circumference and 42 along the midsection (16×42) of 1000 mm, ℓ_e is roughly 24 mm – giving a crude estimate of $\Delta t_{\text{cr}} \approx 4.65$ μs, which suggests a number of iterations of the order of 10^8. Using double precision is therefore critical in order to avoid round-off errors.

The mass scaling results are presented in Table 3 and Fig. 9. Five different mass scaling factors were used (1, 10^2, 10^4, 10^6, and 10^8). According to Eqs. (6) and (7) the theoretical speedup from using a mass scaling factor M is $\sqrt{M}$, which means that increasing the mass by 10^2 times should speed up the simulation by a factor of 10. This is captured well by the simulations as seen in Table 3, particularly the number of iterations scales almost perfectly. In addition, the peak force and the average force, F_{peak} and $\bar{F}$ respectively, are listed along with the energy ratio (kinetic energy E_{kin} to total energy E_{tot}) at the end of the simulation. Ideally the kinetic energy should be close to zero as the deformation is quasi-static, but due to the large mass for the highest scale factor it becomes a significant proportion of the total energy. From these results

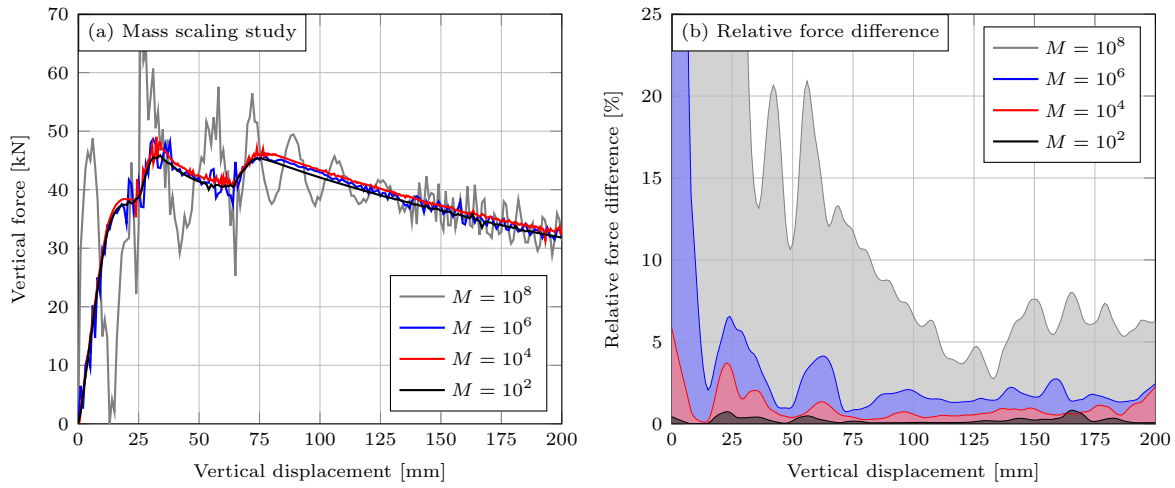

Fig. 9: Simulations of pipe A1 (16×42 mesh) investigating the effect of mass scaling, with (a) showing the force-displacement curves from the contact between the indenter and the pipe using various mass scaling factors M, and (b) illustrating the difference in force level between mass scaled analyses and the unscaled analysis with a 10-point moving average filter.

a mass scaling factor of $M = 10^4$ is judged reasonable. Using no mass scaling is not an option as the CPU time becomes very large even for a coarse mesh like here.

Fig. 9(a) shows the resulting force-displacement curves from the indenter-pipe contact pair in the mass scaling simulations. The simulation using no mass scaling was left out as it was indistinguishable from the one with $M = 10^2$. Here it is obvious that $M = 10^8$ is useless as the large mass introduces too large oscillations and too much kinetic energy. By looking at the relative force difference between the unscaled and scaled simulations, shown in Fig. 9(b), using $M = 10^6$ causes a too large deviation in the force during the initial stage. The average force deviation $\Delta\bar{F}$ throughout the simulation using $M = 10^6$ is 1.0 kN, while for $M = 10^4$ it is only 0.3 kN. A 10-point moving average smoothing filter has been applied to Fig. 9(b) to remove the most erratic spikes. Based on the discussion above, $M = 10^4$ is thus chosen for further analyses.

4.3. Mesh sensitivity and effect of shell thickness

By gradually increasing the number of elements, a suitable mesh was found. Each mesh is distinguished by the number of elements around the circumference times the number of elements along the 1000 mm long test section. A coarse mesh (16×42), a medium mesh (24×62), a fine mesh (36×92), and an extra fine (36×108) mesh were used. The latter mesh has a refined zone near the contact area, and can be seen in Fig. 10. Transverse force-displacement curves from the mesh sensitivity study are presented in Fig. 11(a), while curves from simulations using different shell thicknesses are plotted in Fig. 11(b). The red curve in Fig. 9(a) is from the same simulation as the red curve in Fig. 11(a). For all cases, the rigid indenter had an element size slightly smaller than the element size in the pipe, thereby making sure that contact is enforced so the pipe cannot penetrate the indenter.

The base thickness for pipe A1 was the experimentally measured value of 4.19 mm. This value was increased and decreased with 0.10 mm two times each. The effect of using different shell thicknesses was

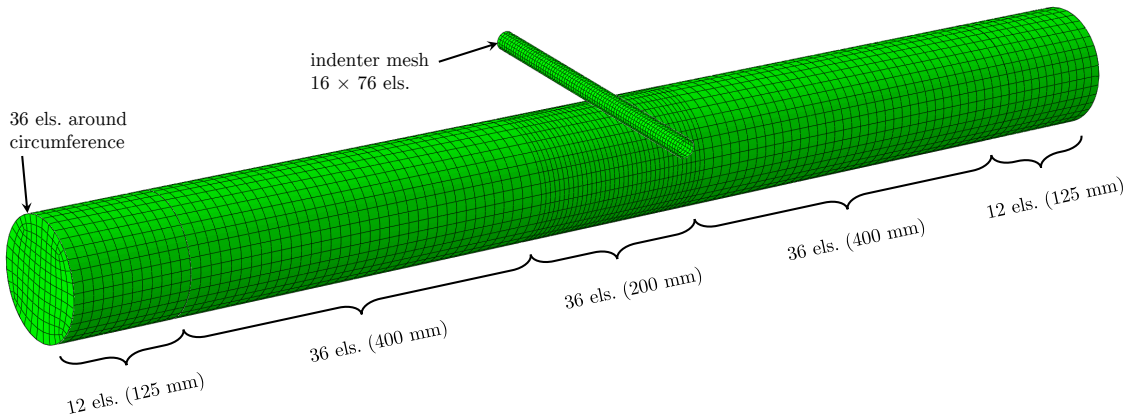

Fig. 10: Final mesh (referred to as 36×108 in Fig. 11(a)) used in simulations, with the center 1.0 m span having 36 elements along the circumference and 108 along the midsection of the pipe. The mesh is refined in the 200 mm contact area.

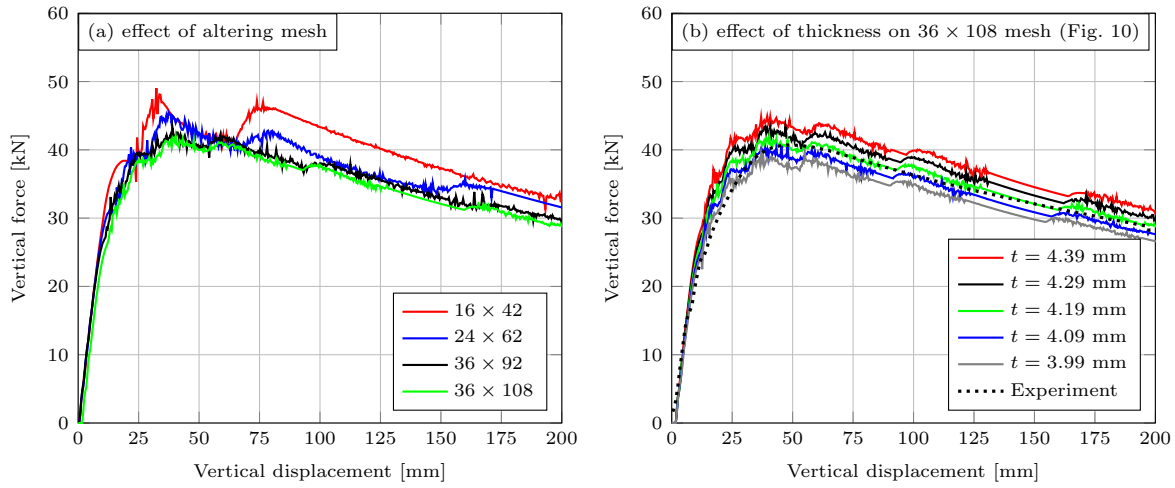

Fig. 11: Explicit simulations ($M = 10^4$) of pipe A1 investigating the effect of refining the mesh (a) and changing the shell thickness (b). The green curves in (a) and (b) are the same.

according to expectations as can be seen in Fig. 11(b), and in line with previous investigations [63]. The equivalent plastic strain at equal levels of transverse deformation was almost the same between the five different thicknesses (about 2% increase from the lowest to the highest thickness). Since the pipes used in the experiments were lathed down from 10 mm thickness to 4 mm thickness in the 1000 mm long test section, some spatial variation in the thickness occurs. As the measured average thickness not necessarily makes the best representation of the pipe as a whole, it can be reverse engineered in the simulations by adjusting the shell thickness. It is possible to create a field representing the thickness according to the measurements across the pipe, but this is left for further work.

While performing the mesh sensitivity study, a somewhat unexpected effect presented itself. All the mesh sizes used for the results in Fig. 11(a) have an even number of elements along the pipe length. This results in a node being placed exactly where the indenter makes first contact with the pipe, i.e., at midspan. Fig. 12 shows a close-up of the dented zone of the pipe at the end of the simulation; the left part has an even number of elements along the test section (42) and the right part has an odd number (43).[2] Having nodes centrically placed and perfectly aligned in both the indenter and the pipe seems to cause more oscillations in the force-displacement curve, which can best be seen in Fig. 13(a). This may be because the contact is at times reduced to a single row of nodes, some which may be in contact while others are not, thereby causing small fluctuations in the contact force. Further, there is a notable difference in the force level during deformation, but this effect disappears when refining the mesh as Fig. 13(b), (c) and (d) attest to. The magnitude of the equivalent plastic strain was throughout the simulation marginally lower when the element number along the longitudinal axis of the pipe was odd, but again the effect was reduced with an increasing

[2]Using 41 elements was also tested, and yielded almost the exact same results as using 43 elements.

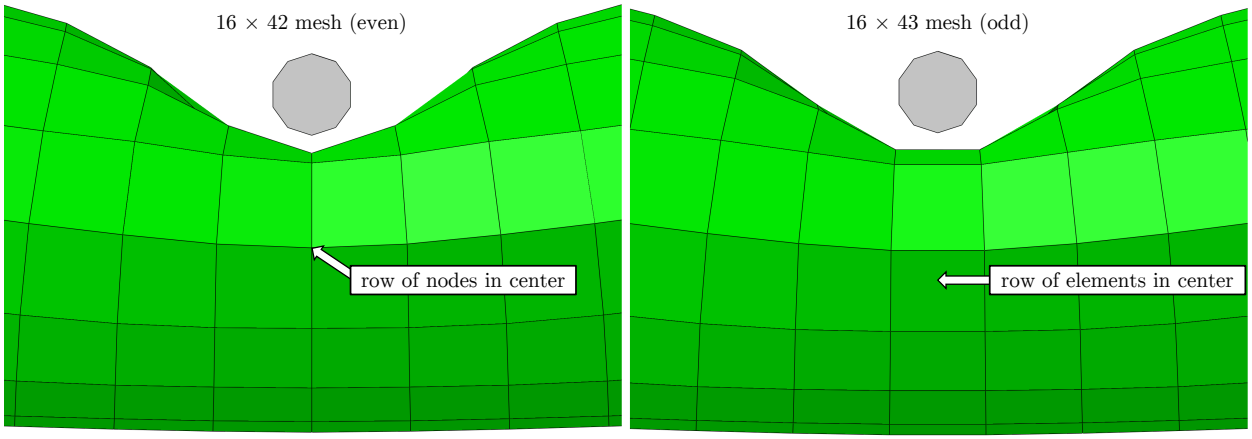

Fig. 12: Even vs. odd number of elements when using the coarse mesh. The apparent gap is due to the shell thickness not being rendered.

number of elements.

Another way of invoking this effect is by rotating the indenter so that the surface normals of the bottom row of indenter elements point directly at the pipe. In Fig. 12 the indenter has a row of nodes facing the pipe, and simulations were run with a row of elements facing the pipe using both even and odd meshes of different grades. The oscillations in the force-displacement curves were similar to even cases in Fig. 13, and some discrepancies in the force levels were noted. No significant differences in deformation was observed due to this. Again, this effect diminished with increasing number of elements. Given that a fairly fine mesh has been chosen (see Fig. 10), a setup with an even number of elements and the indenter position as in Fig. 12 (row of nodes facing the pipe) was chosen for further simulations.

Rather than meshing the indenter it is possible to use an analytic rigid body with a smooth surface. With this technique, the nodes of the pipe are checked for penetration into the analytic rigid body. Simulations of pipe A1 were set up exactly as before, except that an analytic surface was used as the rigid cylinder

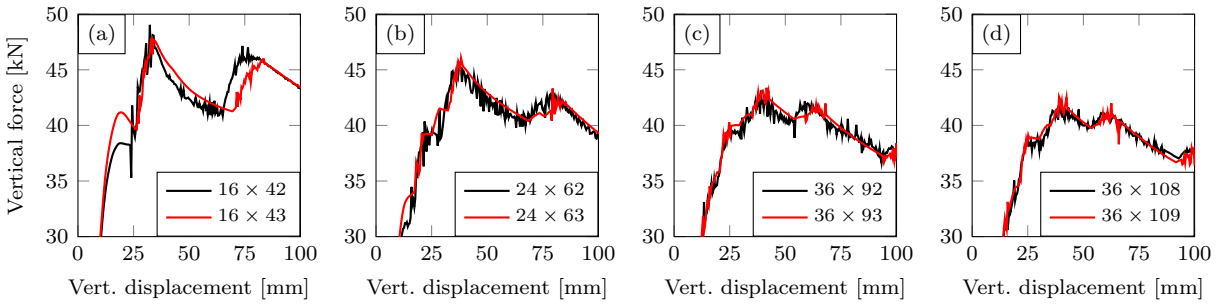

Fig. 13: Force-displacement curves (close to the peak) arising from adding a single row of elements in the axial direction of pipe A1 for different mesh grades in explicit simulations.

indenting the pipe in stead of meshing the indenter. This provides a smooth surface and eliminates the edges caused by the discretisation (see Fig. 12), suggesting that a more even force-displacement curve is produced – which also proved to be the case. Fig. 14 shows the force-displacement curves close to the peak when using an analytic indenter, and the most immediate observation is that the oscillations present in Fig. 13 vanish.

For the coarsest mesh, however, the force-displacement curves are completely off compared with all other cases. The reason for this is that the diameter of the indenter (20 mm) is smaller than the distance between the nodes (about 24 mm). When the number or elements along the pipe length is odd for the coarse mesh (16×43), an element face is placed at midspan (illustrated at the right part of Fig. 12), causing the analytic indenter to avoid the nodes – hence the lack of a red curve in Fig. 14(a). For the even numbered coarse mesh (16×42), a row of nodes is located at midspan making somewhat spurious contact with the indenter.

In all the remaining mesh variations the distance between nodes is always smaller than 20 mm, enabling smooth contact throughout the analyses as indicated by Figs. 14(b)-(d). There is however a slight discrepancy between the red curves (odd numbered) compared with the black (even) caused by the nodal locations; when an element face is situated at midspan (odd) the indenter can penetrate slightly further into the pipe and thereby making contact a little later. Also this effect diminishes when the mesh is refined. Total CPU time was not much affected by using an analytic indenter, but it appeared to decrease slightly as expected.

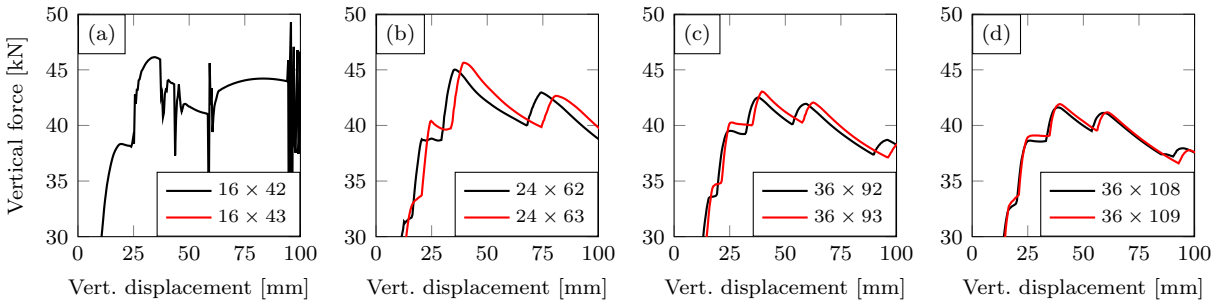

Fig. 14: Force-displacement curves (close to the peak) of pipe A1 simulations using an analytic indenter for different mesh grades.

4.4. Implicit simulations

The main basis for comparison is the force-displacement curves, and further parameters are the geometric measurements after the load sequence as illustrated in Fig. 3. For the implicit simulations general contact is defined using the indenter surface and the surface of the refined portion of the mesh as a surface pair. The time step is limited to 2 s at most when applying the pressure (and constant axial load if relevant), and to 5 s (about 2 mm indenter displacement) during the transverse deformation. Other than that the incrementation is automatic. Key results are listed in Table 4.

The mesh shown in Fig. 10 is used for the implicit and explicit simulations alike. While each increment is much more costly in implicit simulations due to the equilibrium iterations, much fewer increments are needed. For the simulations herein this is an advantage as the physical experiments are quasi-static and take minutes to complete. With contact involved, convergence of the solution may be an issue but for the simulations in this study this did not become a problem.

With 4-node shells (`S4R`), the force-displacement curve in Fig. 15(a) becomes somewhat jagged as each row of elements comes into contact successively. This effect is present in the explicit simulations as well, and can be observed in Fig. 11(a) – particularly for the coarse mesh. Using 8-node second-order shell elements (`S8R` in ABAQUS [36]) ameliorates this effect. The shell thickness was found to have the same effect in the implicit simulations as in the explicit ones (cf. Fig. 11(b)). Using an analytic indenter in the implicit simulations did not have a noticeable effect like in the explicit simulations. Fig. 15(a) includes simulations with both a discretised and an analytic indenter, and the differences are marginal.

The simulations depicted in Fig. 15 were run without parallellisation on a desktop computer, where the simulation using `S8R` elements took about four times longer to complete compared with `S4R` elements. The required memory was approximately doubled. In absolute time, the computer used 12 and 50 minutes for the `S4R` and `S8R` simulations, respectively, meaning that the CPU time is not much of an issue for the implicit simulations compared with the explicit ones. As an alternative, it is possible to run the simulation using 8-node element in the middle area only. This gave just as good results as using 8-node elements all

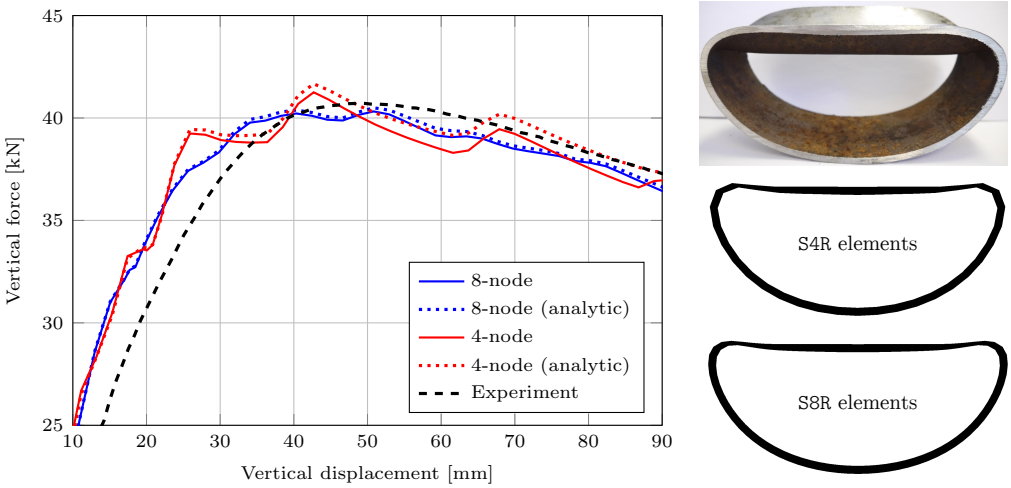

(a) Force-displacement curves using 8-node and 4-node shells (b) Contour of dent

Fig. 15: Implicit simulations of pipe A1 with 8-node and 4-node shell elements. The solid lines in (a) represent the contact between a meshed rigid indenter, while the dotted force-displacement curves are with an analytic indenter. Part (b) shows the contour of the pipe cross-section at midspan using 8-node and 4-node shell elemens compared with the actual test specimen.

Table 4: Comparison between test results (T), explicit simulations (E) and implicit simulations (I). See Fig. 3 for legend.

Pipe →	**A1**	**A2**	**A3**	**P1**	**P2***	**P3**
Parameter	T/ E/ I	T/ E/ I	T/ E/ I	T/ E/ I	T/ E/ I	T/ E/ I
w_i [mm]	120/ 123/ 128	120/ 126/ 127	122/ 126/ 127	117/ 121/ 123	159/ 119/ 121	113/ 120/ 122
ΔL [mm]	31/ 32/ 34	24/ 30/ 32	25/ 31/ 32	32/ 33/ 33	27/ 31/ 31	26/ 31/ 32
$L_{\text{N-N}}$ [mm]	1200/1209/1208	1197/1211/1210	1198/1210/1209	1200/1209/1209	1168/1211/1211	1200/1211/1211
F_{peak} [kN]	40.7/ 41.7/ 40.3	45.9/ 46.2/ 44.5	40.6/ 41.5/ 40.6	47.5/ 50.0/ 48.6	-/ -/ -	-/ -/ -
F_{end} [kN]	28.7/ 28.7/ 27.0	47.0/ 45.7/ 44.4	45.7/ 44.8/ 43.5	45.0/ 43.5/ 44.9	61.1/ 59.1/ 60.8	65.4/ 63.0/ 63.6
α [deg]	8.7/ 9.0/ 9.1	8.5/ 8.9/ 9.0	8.7/ 9.0/ 9.0	9.6/ 9.6/ 9.7	11.6/ 9.6/ 9.7	9.2/ 9.6/ 9.7
p [MPa]	0/ 0/ 0	0/ 0/ 0	0/ 0/ 0	10.3/ 10.3/ 10.3	10.3/ 10.3/ 10.3	10.1/ 10.1/ 10.1
$d_{\text{N-S}}$ [mm]	84/ 76/ 80	89/ 74/ 73	87/ 73/ 72	98/ 91/ 91	90/ 92/ 91	97/ 92/ 91
$d_{\text{E-W}}$ [mm]	164/ 169/ 169	165/ 169/ 169	164/ 169/ 169	152/ 156/ 156	164/ 154/ 154	152/ 155/ 155

*Experimental post-test geometric measurements are inaccurate due to an erroneously applied compressive force after the test.

over, and the simulation took about 25 minutes to complete.

Due to the high curvature in the dent of a deformed pipe, `S8R` elements seem to work better since they are able to maintain a smooth displacement field. This is illustrated in Fig. 15(b), where the contour of the cross-section of the pipe in the middle of the dent is sketched.[3] While the cross-sectional (and global) deformations at the end of the simulations are very similar for the two element types, the strains differ somewhat more. So if a detailed analysis of the strain field is wanted, 8-node elements is the preferred choice. Still, using 4-node elements provides a good prediction for the global force-displacement curve and from there a good estimate of the energy absorption if needed.

Experimental and numerical measurements (both explicit and implicit results using a discretised indenter) are listed in Table 4, and the corresponding simulations are presented in Fig. 16. In general the simulations resemble the experiments closely for all parameters. The explicit results are as described in Section 4.3, while the implicit results are with the `S8R` elements. Generally, the implicit solutions are slightly more compliant due to the increased number of deformation modes (the explicit solutions are restricted to the linear shape functions). The implicit simulation of pipe A2 using 8-node elements is compared with DIC data in Fig. 6, which shows that the results match both qualitatively and quantitatively. Force-displacement curves are shown in Fig. 16, and the overall agreement is very good. The hatched gray areas indicate the lower and upper bounds formed by the minimum and maximum measured pipe wall thicknesses when used in implicit simulations. However, a caveat is made for using global measures to evaluate local performance [64]. It is important to keep in mind what the goal of the results is; estimating the energy absorption or analysing the strain field require two different degrees of precision. These data could also be used to validate analytical or empirical methods, but this is out of scope for the current study.

[3]The circumference using 8-node elements may look slightly rough or edged in Fig. 15(b), but this is only due to a software limitation when rendering the shell thickness.

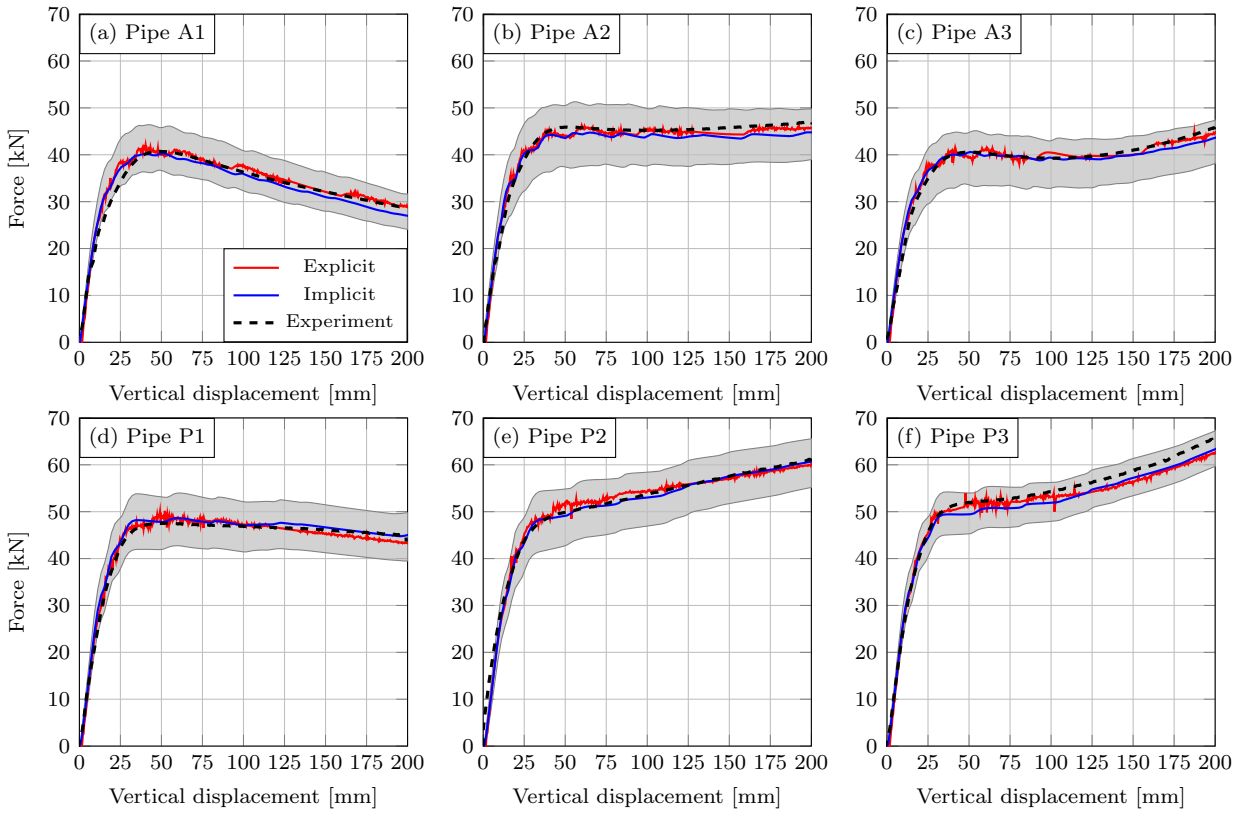

Fig. 16: Force-displacement curves from simulations using the 36×108 mesh and a discretised indenter, for both explicit and implicit simulations. The hatched gray areas indicate the lower and upper bounds formed by the minimum and maximum measured pipe wall thicknesses when used in implicit simulations.

Nevertheless, for both the explicit and implicit solutions, the magnitude of the equivalent plastic strain is lower throughout the simulation when internal pressure is included. Using an implicit simulation without axial loading as an example (a 36×108 mesh with linear elements), a comparison is made with and without internal pressure. With a shell thickness of 4.19 mm for both cases, the equivalent plastic strain ε_{eq} is shown in Fig. 17 for an unpressurised pipe (left) and a pressurised pipe (right). These two cases represent pipe A1 and P1, respectively. In the former, the maximum equivalent plastic strain $\varepsilon_{\text{eq,max}}$ is 0.695 while in the latter $\varepsilon_{\text{eq,max}}$ is 0.625. This result is representative of all simulations, and shows that the internal pressure not only increases resistance to bending, but reduces the strains as well. When a constant axial load is included for pipe A2 and P2, the maximum equivalent plastic strain becomes 0.640 and 0.560, respectively. The corresponding values for A3 and P3 are 0.644 and 0.565. Fig. 17 shows that when pressure is included, the strains distribute across a larger area. The 3D-DIC measurements suggest the same result, but it was difficult to quantify exactly because the area where this effect is most evident is obscured by the indenter and its shadow in the experiments. For future DIC studies of this kind, proper lighting should be ensured.

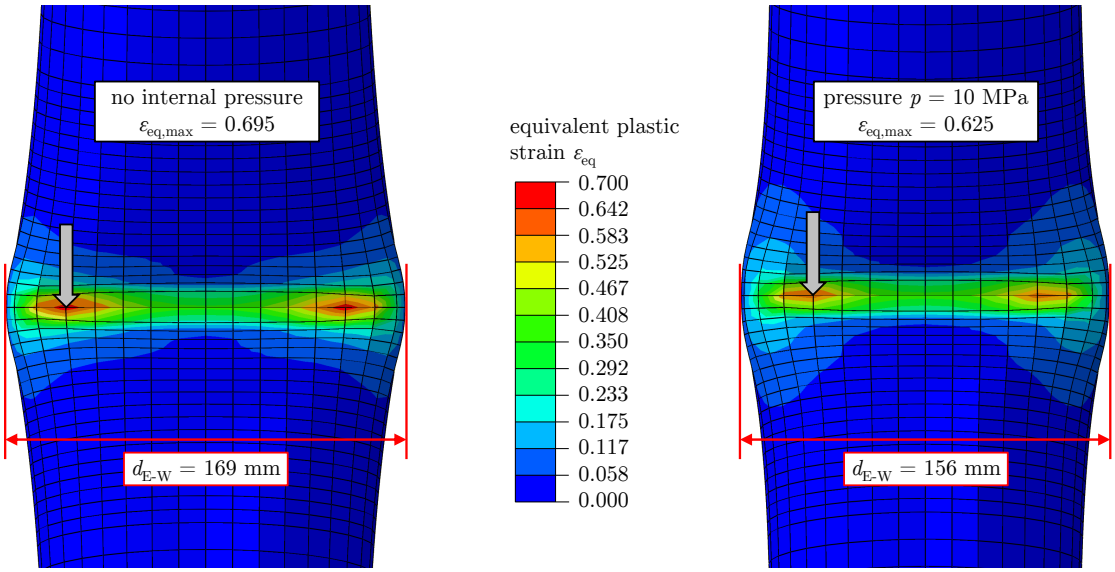

Fig. 17: Comparison of equivalent plastic strain in implicit simulations of A1 (left) and P1 (right) using the 36×108 mesh with linear elements and shell thickness 4.19. The light gray arrows indicate the points with highest equivalent plastic strain.

4.5. Coupled Euler-Lagrange analyses

A variation for the pressure model is made to the explicit setup by modelling the fluid directly. This is done by discretising a $200 \times 340 \times 1400$ mm volume by an Eulerian mesh, and embedding the Lagrangian pipe structure into it. This is called the coupled Eulerian-Lagrangian (CEL) approach in ABAQUS [36]. The Eulerian elements falling inside the structural mesh are given the properties of the desired fluid and the correct pressure is applied by a predefined field, while the remainder of the Eulerian elements are left empty (or "void"). Elements which are intersected by the pipe are given a fill grade from 0 (empty) to 1 (full) based on how much of its volume is located inside the pipe. As the pipe deforms, the fluid is constrained by the boundary of the pipe and the pressure inside is retained.

The Eulerian (fluid) mesh is always discretised finer than the structure to avoid potential problems at the fluid-structure interface [65, 66]. Reduced integration 8-node brick elements have a constant pressure within each element, so making the structural mesh the finest of the two is not advisable if the pressure distribution is of importance. In this case the pressure is constant throughout the test, but the fine fluid mesh is kept to maintain a good resolution of the "location" of the fluid and to minimise numerical diffusion. The fluid is modelled either as a perfect gas, or as a nearly incompressible liquid. The former has the advantage of being insensitive to small volume changes as here, while the latter might suffer a pressure change. It is possible to set up boundary conditions that circumvent this, however this is requires a more in-depth approach, which is beyond the scope of the current study. The main goal is to investigate if modelling the fluid will provide better results or new insight not obtainable from the simpler Lagrangian simulations.

Mass scaling is not applicable with the CEL approach, hence a time scaling factor of 10^{-2} was applied to the simulation time, thus making the simulated time 4.8 s rather than 480 s, which should be equivalent to using $M = 10^4$ for the Lagrangian simulations. Because the fluid elements are always smaller than the solid elements, they govern the critical time step. For the mesh in Fig. 10 the volume measuring $200 \times 340 \times 1400$ mm was discretised by a regular mesh with an element length of 8 mm. With an additional $25 \times 43 \times 175 = 188125$ elements the computational time necessarily increases significantly, so these simulations were run with 48 CPUs on a computing cluster.

By inspecting the results visually, they appear to be quite good qualitatively. Fig. 18(a) shows the fill grade of the fluid in the Eulerian mesh, where 0 is empty (void of fluid) and 1 is full. Around the countours of the pipe some Eulerian elements are only partially filled as the Lagrangian shell elements cut through them. In any case, the fluid follows the structure nicely and the pressure is contained while the deformations are consistent with previous simulations (and with the experiments).

The force-displacement curves arising from the contact between the indenter and the pipe are shown in Fig. 18(b). As in the preceding mass scaled explicit simulations, there are some oscillations, caused by the time scaling and by the meshed indenter. The amplitudes of the oscillations are larger compared with the corresponding Lagrangian simulation (see Fig. 16(d)), which could be due to the time scaling and possible diffusion. In general the force level is decently captured, with a slight change towards the end of the deformation procedure. When a perfect gas equation of state was used, the force dropped slightly. When a Lagrangian pipe element cuts through a Eulerian fluid element, the fluid element is assigned a fluid volume fraction at each node based on its location relative to the pipe. If the volume fraction is below 0.5, contact is not enforced and diffusion ensues. This fact could be the source of the drop in the force when using a perfect gas. For the nearly incompressible liquid, a slight increase was observed at the end of the force-displacement

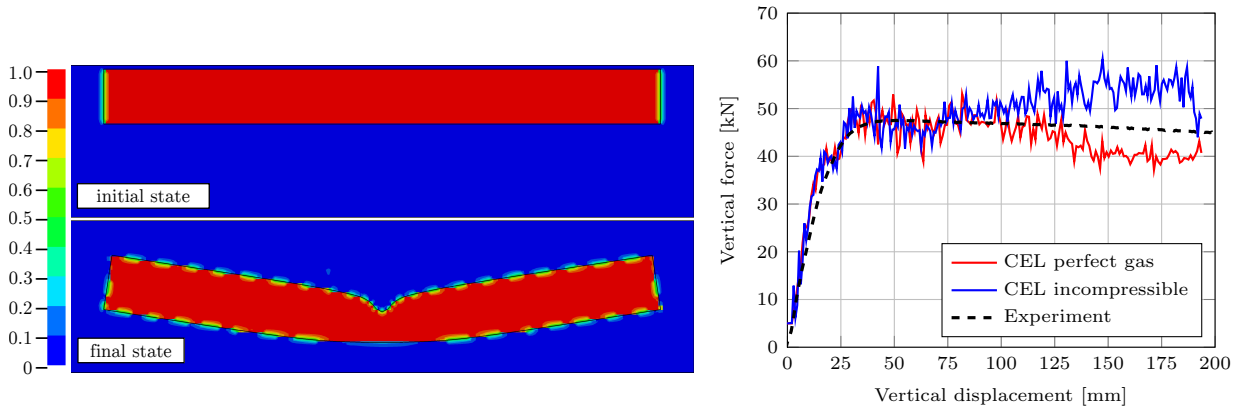

(a) Fill grade of Eulerian elements

(b) Force-displacement curves

Fig. 18: Coupled Euler-Lagrange simulation of pipe P1.

curve. This increase is most likely due to the build-up of pressure caused by the decrease in volume of the pipe during deformation, thus counteracting the diffusion effect. The CPU time for the CEL analyses with a time scale factor of 10^{-2} was about 12 hours when running 48 CPUs in parallel.

5. Discussion

The X65 material used in this study is both isotropic and homogeneous [7], and the chosen material model appears to provide sufficient accuracy for the global simulations. As expected, three-point bending tests on circular pipes show that including an internal pressure increases the force required to reach a certain deformation. Also, the deformed cross-sectional shape is less ovalised after the test procedure when internal pressure is included, with a more localised dent as noted by Jones and Birch [30]. Applying a constant axial force while simultaneously bending pipes further increases the resisting force when deforming the pipe transversely. Using an axial load which increases linearly with the transverse deformation, shows that the effect of increased resistance is greater for greater values of the axial load as one would expect. The sequence in which the loads are applied can be important – if the axial force is applied after the transverse deformation, resulting in a compression-tension load in critical areas of the dent, the likelyhood of fracture increases significantly for this material [7, 42]. Investigations using an optical light microscope showed no signs of fracture in the pipes despite the large deformation. This is partly due to the high ductility of the material. The most contributing factor, however, appears to be that the tests are quasi-static. During an impact event, fracture typically occurs during the elastic springback because a rapid reversal of the load can load to a ductile-to-brittle transition [7, 67].

After having established a good mesh and a reasonable mass scaling factor, the explicit finite element simulations were able to capture the global behaviour very well, both in terms of force-displacement curves and initial system stiffness. The thickness of the pipes is important in order to obtain the correct force level. As the pipes were lathed down from 10 mm to about 4 mm, this caused a somewhat uneven thickness which is not necessarily well represented by a uniform shell thickness in the simulations although a good approximation is obtained. Using the maximum and minimum measured thicknesses creates an upper and lower band of the experimental force-displacement data, illustrated by the hatched areas in Fig. 16. Experimental and numerical data are listed in Table 4, where it is observed that the numerical values are close to the experimental observations. It is interesting to see that for both the tests and the simulations, the deformation values for the linearly increasing axial load are typically between the case with no axial load and the case with a constant axial load. In addition, the DIC results agreed well with the numerical data, both qualitatively and quantitatively, thus suggesting that strain fields obtained by the simulations resemble reality quite well. This result means that the numerical simulations can be used as good and reliable predictors for e.g. stress triaxiality, strain history or other parameters closely linked to failure.

Using an odd or even number of elements along the axial direction of the pipe resulted in notable differences in the force level during deformation, but this effect disappeared with increased mesh refinement. More oscillations were present using an even number, which suggests that care must be taken when utilising symmetry, particularly for a coarse mesh. Using an analytic indenter was a failure for the coarsest mesh as the diameter of the indenter was smaller than the nodal distance, allowing the indenter to pass through the pipe mesh (see Fig. 14(a)) as the analytic rigid body has no nodes. For the finer mesh grades, the analytic approach worked well, providing a more even contact without causing oscillations (compare Fig. 13 with Fig. 14).

The implicit simulations were also able to recreate the experiments with good accuracy. By using `S8R` elements the force-displacement curve becomes more even, and a smooth displacement field was obtained. Also, the odd or even problem discussed above was negligible. With a runtime only a fraction of the explicit counterpart, an implicit scheme is superior for simulating the experiments in this study. Using a discretised rigid indenter or an analytic rigid indenter did not affect the results to any significant extent for the implicit simulations, as can be seen in Fig. 15(b). The points with the highest equivalent plastic strain – coinciding with points where fracture has been observed in similar experiments from previous work [7] – were analysed in more detail. Stress triaxiality data was extracted from these points (shown in Fig. 17), and plotted against the equivalent plastic strain in Fig. 19. It is observed that the strain paths are very similar for all cases, and the major difference is the strain at the end of the simulation (indicated by a cross shaped marker). The diamond shaped markers show the point when the plastic hinge passes through the evaluated point, while the circular markers indicate when the indenter comes into contact with said point. When pressure is included, the stress triaxiality is generally lower for the same magnitude of equivalent plastic strain. The indenter also makes contact with the critical point at an earlier stage compared with the ambient pipes

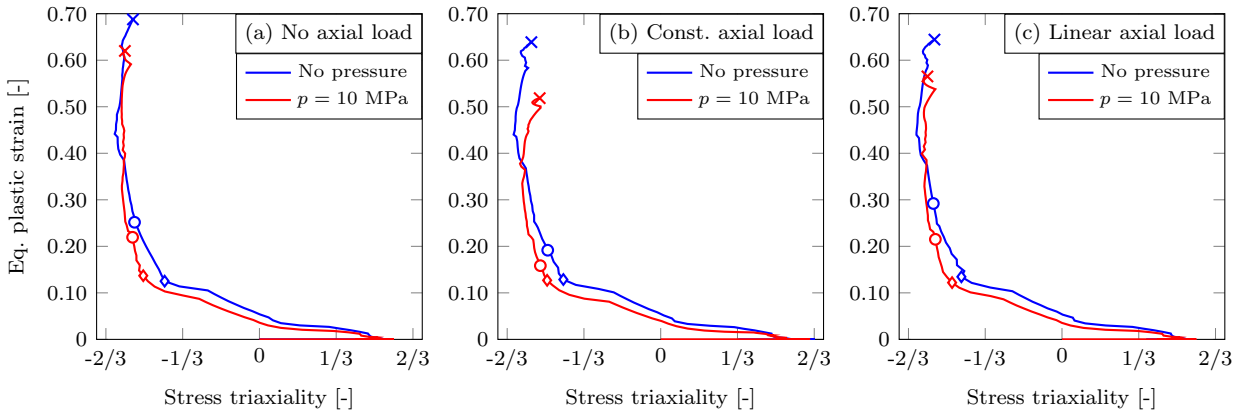

Fig. 19: Stress triaxiality data extracted from the most critical point (see Fig. 17) in implicit simulations using 4-node shell elements. The cross shaped markers indicate the end of the simulation.

becuase the critical point is closer to the center for the pressurised pipes.

The stress triaxiality starts out at approximately 0.5 when the material point first yields. As the travelling plastic hinge arrives at the evaluated point, the plastic strains start to increase. After the indenter makes contact with the point, the triaxiality remains fairly constant at about -0.6. Large compressive strains prior to tension may as mentioned cause a ductile-to-brittle transition [7, 67], which can be devastating to the pipeline integrity. A more detailed analysis of compression-tension loading has been carried out [42], and this work could be extended to a pipe impact scenario to assess the probability of fracture.

As the pressures used herein are constant throughout the test, a numerical representation by application of a uniform pressure load on the internal surface of the pipe is sufficient, and this is the typical approach in the literature [68]. Using an Eulerian mesh to this end is not necessary, as this technique is mostly intended for problems like fluid flow or liquid sloshing [69]. If, however, the change in volume during deformation alters the pressure, using some kind of fluid-structure interaction is helpful [44]. Another approach is to mesh only the interior of the pipe with a mesh that is able to follow the deformation of the pipe (arbitrary Lagrangian-Eulerian method), thereby reducing the number of required fluid elements. When comparing the pressurised simulations with their unpressurised equivalents, the magnitude of the equivalent plastic strain was always lower when pressure was included.

6. Conclusions

After investigating material and component tests of X65 steel pipes it can be concluded that the material is homogeneous and isotropic, and is well represented by a simple power law. A tensile axial force increases a pipe's resistance to transverse bending, but does not seem to have a significant influence on the deformed shape of the pipe after unloading. Internal pressure increases the resistance to transverse bending as well, and can decrease the ovalisation of the pipe's cross-section. Strain measurements by DIC gave decent results, but it was difficult to discern the six different tests based on strains alone because the most strained area revealing potential differences was obscured by the indenter. No fracture was observed in the pipes due to the quasi-static deformation rate used.

Finite element simulations are able to recreate the experiments closely, including the effect of the axial load and the internal pressure. The thickness of the pipes is important, and lower and upper bounds on the transverse force-displacement curve are created by the minimum and maximum measured thicknesses respectively. Using an odd or an even number of elements along the axial direction of the pipe can influence the force level if the mesh is coarse. Discretising the indenter by rigid elements could cause oscillations in the force-displacement curves, especially when nodes collided heads on. Analytic rigid surfaces amends this problem, but requires a sufficiently fine mesh to allow detection of contact. The effects of indenter representation were mainly limited to explicit simulations. The stress triaxiality is first tensile in the most

critical point, and is then reversed into compression where most of the plastic straining takes place.

A coupled Eulerian-Lagrangian approach may capture fluid flow and pressure changes, but is not necessary when the pressure is constant. For this problem, where the deformation is quasi-static and higher-order accuracy may be needed due to high strain gradients, an implicit scheme is recommended over an explicit scheme as it takes much less time to complete a calculation and no mass scaling is needed. In addition, higher-order elements are available.

Acknowledgements

The authors gratefully appreciate the financial support from NTNU and the Research Council of Norway through the Centre for Advanced Structural Analysis, Project No. 237885 (CASA). Thankful acknowledgement is made to Dr. Ing. Håvar Ilstad and Dr. Ing. Erik Levold at Statoil ASA for their contributions and for supplying the test material.

References

[1] N. Jones, R. Birch, Impact behaviour of pressurised pipelines, Structures Under Shock and Impact X (2008) 219–228.

[2] V. Longva, S. Sævik, E. Levold, H. Ilstad, Dynamic simulation of subsea pipeline and trawl board pull-over interaction, Marine Structures 34 (2013) 156–184.

[3] L. Oosterkamp, D. Hilding, H. Ilstad, Numerical Modelling of Impact to Pipelines by Real Geometry Trawl Gear using LS-DYNA, Proceedings of the 27th International Ocean and Polar Engineering Conference, San Francisco, USA (2017) 214–219.

[4] DNV GL AS, Offshore standard DNV-RP-F111: Interference between trawl gear and pipelines, Det Norske Veritas Germanischer Lloyd AS, 2014.

[5] M. Kristoffersen, T. Børvik, M. Langseth, H. Ilstad, E. Levold, O. Hopperstad, Damage and failure in an X65 steel pipeline caused by trawl gear impact, Proceedings of the ASME 2013 32nd International Conference on Ocean, Offshore and Arctic Engineering, Nantes, France (2013). Paper no. 11277.

[6] A. Manes, R. Porcaro, H. Ilstad, E. Levold, M. Langseth, T. Børvik, The behaviour of an offshore steel pipeline material subjected to stretching and bending, Ships and Offshore Structures 7 (2012) 371–387.

[7] M. Kristoffersen, T. Børvik, I. Westermann, M. Langseth, O. Hopperstad, Impact against X65 steel pipes – An experimental investigation, International Journal of Solids and Structures 50 (2013) 3430–3445.

[8] P. Bergan, E. Mollestad, Impact-Response Behaviour of Offshore Pipelines, Journal of Energy Resources Technology 104 (1982) 325–329.

[9] B. Liu, C. Soares, Plastic response and failure of rectangular cross-section tubes subjected to transverse quasi-static and low-velocity impact, International Journal of Mechanical Sciences 90 (2015) 213–227.

[10] Z. Wang, K. Liu, C. Ji, D. Chen, G. Wang, C. Soares, Experimental and numerical investigations on the T joint of jack-up platform laterally punched by a knife edge indenter, Ocean Engineering 127 (2016) 212–225.

[11] N. Jones, S. Birch, R. Birch, L. Zhu, M. Brown, An experimental study on the lateral impact of fully clamped mild steel pipes, Proceedings of the Institution of Mechanical Engineers, Part E: Journal of Process Mechanical Engineering (1992) 111–127.

[12] B. Cerik, H. Shin, S.-R. Cho, A comparative study on damage assessment of tubular members subjected to mass impact, Marine Structures 46 (2016) 1–29.

[13] C. Soares, T. Søreide, Plastic Analysis of Laterally Loaded Circular Tubes, Journal of Structural Engineering 109 (1983) 451–467.

[14] J. Travanca, H. Hao, Numerical analysis of steel tubular member response to ship bow impacts, International Journal of Impact Engineering 64 (2014) 101–121.

[15] S. Thomas, S. Reid, W. Johnson, Large deformations of thin-walled circular tubes under transverse loading – I: An experimental survey of the bending of simply supported tubes under a central load, International Journal of Mechanical Sciences 18 (1976) 325–333.

[16] K. Chen, W. Shen, Further experimental study on the failure of fully clamped steel pipes, International Journal of Impact Engineering 21 (1998) 177–202.

[17] N. Jones, W. Shen, A theoretical study of the lateral impact of fully clamped pipelines, Proceedings of the Institution of Mechanical Engineers, Part E: Journal of Process Mechanical Engineering (1992).

[18] L. Zhu, Q. Liu, N. Jones, M. Chen, Experimental study on the deformation of fully clamped pipes under lateral impact, International Journal of Impact Engineering 111 (2018) 94–105.

[19] C. Ng, W. Shen, Effect of lateral impact loads on failure of pressurised pipelines supported by foundation, Proceedings of the Institution of Mechanical Engineers 220 (E) (2006) 193–206.

[20] A. Palmer, M. Touhey, S. Holder, M. Anderson, S. Booth, Full-scale impact tests on pipelines, International Journal of Impact Engineering 32 (2006) 1267–1283.

[21] O. Vestrum, M. Kristoffersen, M. Langseth, T. Børvik, H. Ilstad, M. Polanco-Loria, Quasi-static and dynamic deformation of polymer coated pipes, Proceedings of the ASME 2017 36th International Conference on Ocean, Offshore and Arctic Engineering, Trondheim, Norway (2017). Paper no. 62506.

[22] J. Wilhoit, J. Merwin, The Effect of Axial Tension on Moment Carrying Capacity of Line Pipe Stressed Beyond the Elastic Limit, Offshore Technology Conference OTC 1355 (1971).

[23] J. Dyau, S. Kyriakides, On the Response of Elastic-Plastic Tubes Under Combined Bending and Tension, Journal of Offshore Mechanics and Arctic Engineering 114 (1992) 50–62.

[24] Y. Bai, R. Igland, T. Moan, Ultimate Limit States of Pipes Under Combined Tension and Bending, International Journal of Offshore and Polar Engineering 4 (1994) 312–319.

[25] Y. Wang, D. Gao, J. Fang, On the Buckling Response of Offshore Pipelines under Combined Tension, Bending and External Pressure, Computers, Materials & Continua 48 (2015) 25–42.

[26] S. Kyriakides, E. Corona, Pipe Collapse Under Combined Pressure, Bending, and Tension Loads, Offshore Technology Conference, Houston, Texas, USA (1989) 541–550. Paper no. OTC 6104.

[27] Y. Bai, R. Igland, T. Moan, Tube Collapse Under Combined Pressure, Tension and Bending Loads, International Journal of Offshore and Polar Engineering 3 (1993) 121–129.

[28] T. Moan, S. Estefen, S. Sævik, R. Zimmer, Limit States for the Ultimate Strength of Tubulars Subjected to Pressure, Bending and Tension Loads, Marine Structures 7 (1994) 323–344.

[29] S.-R. Cho, Q.-T. Do, H.-K. Shin, Residual strength of damaged ring-stiffened cylinders subjected to external hydrostatic pressure, Marine Structures 56 (2017) 186–205.

[30] N. Jones, R. Birch, Influence of internal pressure on the impact behaviour of steel pipelines, International Journal of Pressure Vessel Technology 118 (1996) 464–471.

[31] J. Liu, A. Francis, Theoretical analysis of local indentation on pressurised pipes, International Journal of Pressure Vessels and Piping 81 (2004) 931–939.

[32] S. Karamanos, K. Andreadakis, Denting of internally pressurized tubes under lateral loads, International Journal of

Mechanical Sciences 48 (2006) 1080–1094.

[33] M. Kristoffersen, T. Børvik, M. Langseth, H. Ilstad, E. Levold, Transverse deformation of pressurised pipes with different axial loads, Proceedings of the ASME 2017 36th International Conference on Ocean, Offshore and Arctic Engineering, Trondheim, Norway (2017). Paper no. 62507.

[34] I. Iflefel, D. Moffat, J. Mistry, The interaction of pressure and bending on a dented pipe, International Journal of Pressure Vessels and Piping 82 (2005) 761–769.

[35] Y. Bai, R. Igland, T. Moan, Tube Collapse Under Combined External Pressure, Tension and Bending, Marine Structures 10 (1997) 389–410.

[36] Abaqus user's manual version 6.14, SIMULIA, 2016.

[37] M. Kristoffersen, T. Børvik, M. Langseth, O. Hopperstad, X65 steel pipes subjected to combined stretching and bending, MARINE 2015 - Computational Methods in Marine Engineering VI, Rome, Italy (2015) 1004–1014.

[38] C.-K. Oh, Y.-J. Kim, J.-H. Baek, W.-S. Kim, Development of stress-modified fracture strain for ductile failure of API X65 steel, International Journal of Fracture 143 (2007) 119–133.

[39] A. Ghiotti, S. Fanini, S. Bruschi, P. Bariani, Modelling of the Mannesmann effect, CIRP Annals - Manufacturing Technology 58 (2009) 255–258.

[40] M. Fourmeau, T. Børvik, A. Benallal, O. Hopperstad, Anisotropic failure modes of high-strength aluminium alloy under various stress states, International Journal of Plasticity 48 (2013) 34–53.

[41] C. Soret, Y. Madi, V. Gaffard, J. Besson, Local approach to fracture applied to the analysis of a full size test on a pipe containing a girth weld defect, Engineering Failure Analysis (2017). http://dx.doi.org/10.1016/j.engfailanal.2017.07.035.

[42] M. Kristoffersen, T. Børvik, O. Hopperstad, Using unit cell simulations to investigate fracture due to compression-tension loading, Engineering Fracture Mechanics 162 (2016) 269–289.

[43] S. Ehlers, E. Østby, Increased crashworthiness due to arctic conditions – The influence of sub-zero temperature, Marine Structures 28 (2012) 86–100.

[44] M. Kristoffersen, F. Casadei, T. Børvik, M. Langseth, O. Hopperstad, Impact against empty and water-filled X65 steel pipes – Experiments and simulations, International Journal of Impact Engineering 71 (2014) 73–88.

[45] R. Hill, The Mathematical Theory of Plasticity, Oxford University Press, 1950.

[46] G. Le Roy, J. Embury, M. Ashby, A model of ductile fracture based on the nucleation and growth of voids, Acta Metallurgica 29 (1981) 1509–1522.

[47] E. Gjertveit, J. Berge, B. Opheim, The Kvitebjørn Pipeline Repair, Offshore Technology Conference, Houston, Texas, USA (2010). Paper no. OTC 20814.

[48] A. Clausen, Stretch Bending of Aluminium Extrusions, Ph.D. thesis, Norwegian University of Science and Technology, 1999.

[49] A. Palmer, A. Neilson, S. Sivadasan, Pipe perforation by medium-velocity impact, International Journal of Impact Engineering 32 (2006) 1145–1157.

[50] A. Gresnigt, S. Karamanos, K. Andreadakis, Lateral loading of internally pressurized steel pipes, Journal of Pressure Vessel Technology 129 (2007) 630–638.

[51] F. Irgens, Continuum mechanics, Springer Verlag, 2008.

[52] M. Zeinoddini, J. Harding, G. Parke, Effect of impact damage on the capacity of tubular steel members of offshore structures, Marine Structures 11 (1998) 141–157.

[53] N. Jones, R. Birch, Low-velocity impact of pressurised pipelines, International Journal of Impact Engineering 37 (2010) 207–219.

[54] Q. Shah, Experimental and numerical study on the orthogonal and oblique impact on water filled pipes, International

Journal of Impact Engineering 38 (2011) 330–338.

[55] Y. Dou, Y. Liu, Computational investigation of lateral impact behavior of pressurized pipelines and influence of internal pressure, Thin-Walled Structures 95 (2015) 40–47.

[56] J.-H. Baek, Y.-P. Kim, W.-S. Kim, J.-M. Koo, C.-S. Seok, Load bearing capacity of API X65 pipe with dent defect under internal pressure and in-plane bending, Materials Science and Engineering A 540 (2012) 70–82.

[57] J. Johnsen, F. Grytten, O. Hopperstad, A. Clausen, Experimental set-up for determination of the large strain tensile behaviour of polymers at low temperatures, Polymer Testing 53 (2016) 305–313.

[58] M. Kristoffersen, J. Pettersen, V. Aune, T. Børvik, Experimental and numerical studies of the structural response of normal strength concrete slabs subjected to blast loading, Submitted for possible journal publication (under review). (2018).

[59] E. Fagerholt, Field measurements in Mechanical Testing Using Close-Range Photogrammetry and Digital Image Analysis, Ph.D. thesis, Norwegian University of Science and Technology, 2012.

[60] M. Kristoffersen, T. Børvik, M. Langseth, O. Hopperstad, Dynamic versus quasi-static loading of X65 steel pipes, European Physical Journal – Special Topics 225 (2016) 325–334.

[61] D.-H. Yoo, B.-S. Jang, K.-H. Yim, Nonlinear finite element analysis of failure modes and ultimate strength of flexible pipes, Marine Structures 54 (2017) 50–72.

[62] T. Wierzbicki, M. Suh, Indentation of tubes under combined loading, International Journal of Mechanical Sciences 30 (1988) 229–248.

[63] M. Kristoffersen, F. Casadei, T. Børvik, M. Langseth, G. Solomos, O. Hopperstad, Numerical simulations of submerged and pressurised X65 steel pipes, XII International Conference on Computational Plasticity, Barcelona, Spain (2013).

[64] K. Mathisen, K. Okstad, T. Kvamsdal, S. Raknes, Simulation of contact between subsea pipeline and trawl gear using mortar-based isogeometric analysis, MARINE 2015 - Computational Methods in Marine Engineering VI, Rome, Italy (2015).

[65] F. Casadei, S. Potapov, Permanent fluid-structure interaction with non-conforming interfaces in fast transient dynamics, Computer Methods in Applied Mechanics and Engineering 193 (2004) 4157–4194.

[66] V. Aune, G. Valsamos, F. Casadei, M. Larcher, M. Langseth, T. Børvik, Use of damage-based mesh adaptivity to predict ductile failure in blast-loaded aluminium plates, Procedia Engineering 197 (2017) 3–12.

[67] J. Ludley, D. Drucker, A Reversed-Bend Test to Study Ductile to Brittle Transition, Welding Journal (Research Supplements) 39 (1960) 543–546.

[68] Y. Dou, Y. Liu, Analytical investigation and parametric study of lateral impact behavior of pressurized pipelines and influence of internal pressure, International Journal for Computational Methods in Engineering Science and Mechanics (2017). DOI: 10.1080/15502287.2017.1350215.

[69] S. Malenica, L. Diebold, S. Kwon, D.-S. Cho, Sloshing assessment of the LNG floating units with membrane type containment system where we are?, Marine Structures 56 (2017) 99–116.